AIAA JOURNAL
Vol. 46, No. 4, April 2008

Stability Analysis of Solid Rocket Motor Combustion by Computational Fluid Dynamics

Toru Shimada*
Japan Aerospace Exploration Agency,
Kanagawa 229-8510, Japan
and
Masahisa Hanzawa,† Takakazu Morita,‡ Takashi Kato,§ Takashi Yoshikawa,¶ and
Yasuhiko Wada**
Tokai University, Kanagawa 259-1292, Japan

DOI: 10.2514/1.31976

The acoustic combustion instability of a solid rocket motor is investigated by computational fluid dynamics and compared with theoretical results. The quasi-one-dimensional Euler equations for the unsteady flow inside the combustion chamber and the equation for the thermal conduction inside the solid propellant are simultaneously solved with a quasi-steady flame model near the burning surface. The Runge–Kutta discontinuous Galerkin method is used as the platform for the flow simulation, and a numerical accuracy study is carried out. The conventional second-order finite volume method is verified to give accurate results by comparison with the third-order Runge–Kutta discontinuous Galerkin method. The growth rate versus the nozzle entrance Mach number for the attenuation case shows good agreement with the linear theory. For the growing case, it is shown that agreement is good for small Mach numbers. The results of the stability limit show good agreement with the theory for low Mach numbers. For higher Mach numbers, the stability-limit curve of the present simulation shows a dependency on the imaginary part of the response function. Extension to the axisymmetric problem is straightforward, and preliminary results are obtained.

Nomenclature

a	=	speed of sound
c	=	specific heat
c^*	=	characteristic exhaust velocity
c_p	=	specific heat at constant pressure
D	=	mass diffusion coefficient
E	=	total energy per unit volume of fluid
E_S	=	activation energy of surface reaction
f	=	frequency
$\mathbf{f}$	=	convection flux vector
H	=	total enthalpy
M_b	=	burning surface Mach number
M_N	=	nozzle entrance Mach number
m_b	=	mass generation rate from the burning surface
p	=	pressure
Q	=	heat release of the gas reaction per unit mass
Q_S	=	heat release of the surface reaction per unit mass
$\mathbf{q}$	=	conservation quantity vector
R	=	gas constant, radius
R_p	=	pressure-coupled response function
$\dot{r}_b$	=	linear burning rate
$\mathbf{S}$	=	source term vector
T	=	temperature
t	=	time
u, v	=	velocity
$\dot{w}^{(P)}$	=	product mass generation due to gas reaction
x	=	axial location
y	=	location normal to the burning surface
α	=	growth rate
α_s	=	thermal diffusivity of the propellant
γ	=	specific heat ratio
η	=	nondimensional acoustic pressure
λ	=	thermal conductivity
ν	=	reaction order
ξ	=	transformed space coordinate
ρ	=	density

Subscripts

C	=	chamber
E	=	nozzle exit
F	=	fuel
f	=	flame
N	=	nozzle
O	=	oxidizer
P	=	product
s	=	solid phase
T	=	throat
$'$	=	small perturbation
$\hat{}$	=	nondimensional quantity

Presented as Paper 2007-3427 at the 13th AIAA/CEAS Aeroacoustics Conference, Rome, 21–23 May 2007; received 5 May 2007; revision received 23 October 2007; accepted for publication 4 December 2007.

*Professor, Department of Space Transportation Engineering, Institute of Space and Astronautical Science, 3-1-1 Yoshinodai, Sagamihara. Senior Member AIAA.

†Professor, Department of Aeronautics and Astronautics, Faculty of Engineering, 1117 Kitakaname, Hiratsuka.

‡Lecturer, Department of Aeronautics and Astronautics, Faculty of Engineering, 1117 Kitakaname, Hiratsuka.

§Graduate Student, Department of Aeronautics and Astronautics, Faculty of Engineering, 1117 Kitakaname, Hiratsuka; currently Engineer, Automobile R&D Center, Honda R&D Co., Ltd.

¶Graduate Student, Department of Aeronautics and Astronautics, Faculty of Engineering, 1117 Kitakaname, Hiratsuka; currently Engineer, Advanced Technical Development Division, Daihatsu Motor Co., Ltd.

**Graduate Student, Department of Aeronautics and Astronautics, Faculty of Engineering, 1117 Kitakaname, Hiratsuka; currently Engineer, Engineering Department Mechanical Systems, Narita International Airport Corporation.

Superscripts

(F) = fuel
(O) = oxidizer
(P) = product

I. Introduction

THE oscillatory combustion of a solid rocket motor (SRM) is classified into acoustic combustion instability and nonacoustic instability. The acoustic combustion instability, which is caused by the resonance between the natural acoustic oscillation of the flow and the fluctuation of the propellant burning rate in the combustion chamber, causes the increase of the average burning rate and the combustion pressure.

The theoretical analysis of the combustion instability is divided into linear analyses and nonlinear analyses. A linear analysis is usually based on the small-perturbation method, and the application of the theory is limited to the case of small-amplitude oscillations. On the other hand, a nonlinear analysis is done for a finite amplitude oscillation. Although much recent research handles nonlinear problems, the linear analysis is also important, because a nonlinear phenomenon is often the result of the amplification of minute acoustic oscillations.

In the past decades, the ability of computational technology has improved greatly. Research on the combustion instability of SRMs is heading for advanced simulations of multidimensional, turbulent, and multiphase flows [1,2].

In this research, the main attention is paid on the axial-mode acoustic stability of an SRM. In dealing with the axial-mode acoustics, the quasi-one-dimensional (Q1D) Euler equations for the unsteady flow inside the combustion chamber and the equation for the thermal conduction inside the solid propellant are simultaneously solved with a combustion model at the burning surface. The attenuation and the amplification of the acoustic waves inside the chamber are simulated by this method, and the stability limit and the growth rate are evaluated. To evaluate the validity of the mathematical model, several numerical methods are employed to compare the results among them. The solutions are compared with the linear analysis results at the same time. Compared are the four numerical methods for the flow analysis, such as the Runge–Kutta discontinuous Galerkin (RKDG) methods of the first, second, and third orders and the second-order finite volume method (FVM). Currently, the unsteady thermal conduction is commonly treated by the second-order finite difference method with exponential coordinate-system transformation.

In the following sections of the paper, the mathematical model will first be described and then the numerical results will be shown. Discussion will be made on the stability boundary and the growth rates versus the activation energy and the heat release of the surface reaction and the nozzle entrance Mach number. Also, discussion will be made on the difference between the nonlinear numerical results and the linear theoretical results and on the effect of the numerical scheme precision on the results. Finally, the extension of the analysis to the axisymmetric flows will be briefly described with other future topics.

II. Method of Analysis

A. Mathematical Model

1. Solid Rocket Motor Configuration

Although the real combustion gas in SRMs consists of various gas species and molten-liquid droplets of aluminum and alumina, only the single-species gas phase is considered here. The importance of the particulates in the acoustics in SRMs is well-recognized and it should be one of the major extensions of the present work. In spite of the single-gas assumption here, it is possible to investigate the validity of the mathematical model and the numerical methods by the use of the theoretical approach.

Let us consider a domain of computation of $0 \le x \le x_E$, where x_E is the location of the nozzle exit, as shown in Fig. 1. The combustion chamber lies in $0 \le x \le x_C$ $(x_C < x_E)$ and a Laval nozzle is connected to the chamber at x_C. The nozzle extends from x_C to x_E with the throat at $x = x_T$. The length of the nozzle is defined as $x_E = 1.2x_C$ to not conflict with applicability of the short nozzle theory [3], which we will use to evaluate the acoustic attenuation at the nozzle entrance. The x_C value is set so that the frequency of the first axial mode of acoustic oscillation is close to the resonance frequency f_r of the solid propellant combustion:

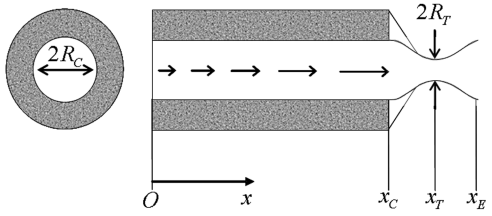

Fig. 1 Configuration of a solid rocket motor.

$$f_r \cong \frac{a_0}{2x_C} \tag{1}$$

where a_0 is the steady-state speed of sound in the chamber. The resonance frequency will be defined from the pressure-coupled response function and described later.

The radius of the port cross section at x is defined as

$$r_C(x) = \begin{cases} R_C & \text{for } 0 \le x \le x_C \\ R_T - \frac{(R_C - R_T)}{(x_C - x_T)^4}(x - x_T)^4 + \frac{2(R_C - R_T)}{(x_C - x_T)^2}(x - x_T)^2 & \text{for } x_C \le x \le x_E \end{cases} \tag{2}$$

where R_T is the throat radius, R_C is the combustion chamber port radius and, at the same time, the radius of the propellant burning surface in this study. Both R_C and R_T are constant for all t.

In the steady state, the mass flow rate is constant for $x_C \le x \le x_B$. Then the following relationship holds:

$$\rho_N u_N \pi R_C^2 = \rho_T u_T \pi R_T^2 \tag{3}$$

where ρ is the density, u is the velocity, and the subscripts N and T represent the nozzle entrance and the throat, respectively.

The velocity can be expressed from the definition of the Mach number as

$$\frac{u_T}{u_N} = \sqrt{\frac{T_T}{T_N}}\frac{1}{M_N} \tag{4}$$

where T is the temperature, and M_N is the Mach number at the nozzle entrance and is less than unity. The Mach number at the throat is set to unity. If one assumes isentropic flow relations within the nozzle, then the following expressions hold:

$$\frac{T_T}{T_N} = \left(\frac{\rho_T}{\rho_N}\right)^{\gamma-1} = \frac{1 + [(\gamma-1)/2]M_N^2}{1 + [(\gamma-1)/2]} \tag{5}$$

where γ is the specific heat ratio of combustion gas.

From Eqs. (3–5), the ratio of R_C/R_T can be determined by the nozzle entrance Mach number as

$$\left(\frac{R_C}{R_T}\right)^2 = \frac{1}{M_N}\left[\frac{2 + (\gamma-1)M_N^2}{\gamma+1}\right]^{\frac{\gamma+1}{2(\gamma-1)}} \tag{6}$$

Moreover, by specifying the combustion temperature T_{f0}, the gas constant R, the mass generation rate from the propellant surface m_{b0}, and the combustion pressure p_c, then we can determine each specific value of R_T and R_C uniquely from

$$\frac{p_c R_T^2}{c^*} = 2m_{b0}R_C x_C, \qquad c^* \equiv \sqrt{\frac{RT_{f0}}{\gamma}\left(\frac{\gamma+1}{2}\right)^{(\gamma+1)/(\gamma-1)}} \tag{7}$$

where subscript 0 refers to the steady-state value.

2. Basic Equations for Fluid Dynamics in the Combustion Chamber and the Nozzle

The governing equations for the fluid dynamics are the Q1D unsteady compressible Euler equations with the mass addition. In a quasi-one-dimensional formulation, the effect of the axial change of the contour of the motor chamber and the nozzle in the source term and in the present case appears as those including $\mathrm{d}r_C/\mathrm{d}x$. The mass addition from the burning surface also appears in the source term as a result of integration over the perimeter boundary of the propellant grain surface. A similar approach has been used and reported in literature [4].

$$\frac{\partial \mathbf{q}}{\partial t} + \frac{\partial \mathbf{f}}{\partial x} = \mathbf{S}, \qquad t \geq 0, 0 \leq x \leq x_E \tag{8}$$

$$\mathbf{q} = \begin{pmatrix} \rho \\ \rho u \\ E \end{pmatrix}, \qquad \mathbf{f} = \begin{pmatrix} \rho u \\ \rho u^2 + p \\ \rho u H \end{pmatrix}$$
$$\mathbf{S} = \frac{2}{r_C(x)} \begin{pmatrix} m_b - \rho u \mathrm{d}r_C/\mathrm{d}x \\ -\rho u^2 \mathrm{d}r_C/\mathrm{d}x \\ m_b c_p T_f - \rho u H \mathrm{d}r_C/\mathrm{d}x \end{pmatrix} \tag{9}$$

where t is the time, ρ is the density, u is the velocity, E is the total energy per unit volume, p is the pressure, H is the total enthalpy, $r_C(x)$ is the radius of the port cross section at x, c_p is the specific heat of combustion gas at the constant pressure, m_b is the mass generation per unit area per unit time due to the solid propellant combustion, and T_f is the flame temperature. The mass addition term is defined as

$$m_b = \begin{cases} \rho_s \dot{r}_b & \text{for } 0 \leq x \leq x_C \\ 0 & \text{for } x_C \leq x \leq x_E \end{cases} \tag{10}$$

where ρ_s is the density of propellant, and $\dot{r}_b$ is the linear burning rate.

Thermodynamic properties of gas and propellant are assumed to be constant for simplicity, and standard relations are assumed:

$$E = \frac{p}{\gamma - 1} + \frac{1}{2}\rho u^2, \qquad H = \frac{E+p}{\rho}, \qquad p = \rho R T_g \tag{11}$$

where γ is the specific heat ratio, R is the gas constant, and T_g is the gas temperature.

The initial condition is defined as

$$\mathbf{q}(x, 0) = \mathbf{q}_0(x) + \mathbf{q}'(x) \tag{12}$$

The first term on the right-hand side is the conserved-value vector at the steady state and is the function that satisfies

$$\left.\frac{\mathrm{d}\mathbf{f}}{\mathrm{d}x}\right|_{\mathbf{q}=\mathbf{q}_0(x)} = \mathbf{S}|_{\mathbf{q}=\mathbf{q}_0(x), m_b=m_{b0}, T_f=T_{f0}} \tag{13}$$

The second term on the right-hand side of Eq. (12) is a small-perturbation vector. It is defined by superimposing the first-mode standing pressure wave to the steady-state pressure field as

$$p(x, 0) = p_0(x) - p' \cos\left(\frac{\pi x}{x_C}\right) \tag{14}$$

where the amplitude p' is set to 0.1% of the combustion pressure p_c.

The boundary conditions at $x = 0$ are for the specularly reflecting wall imposed, assuming that there is an inert wall at the head end; that is,

$$\frac{\partial \rho(0, t)}{\partial x} = \frac{\partial p(0, t)}{\partial x} = u(0, t) = 0 \tag{15}$$

and the supersonic outflow condition is imposed at $x = x_E$. The outflow condition is unsteadily imposed in the numerical simulation: namely, the instantaneous inner-region quantities are extrapolated to the outer ghost cell.

The governing equations for the axisymmetric fluid dynamics for the present case are written as

$$\frac{\partial \mathbf{Q}}{\partial t} + \frac{\partial \mathbf{E}}{\partial x} + \frac{\partial \mathbf{F}}{\partial r} = \mathbf{S}, \qquad t \geq 0, 0 \leq x \leq x_E, 0 \leq r \leq r_C(x) \tag{16}$$

$$\mathbf{Q} = \begin{pmatrix} r\rho \\ r\rho u \\ r\rho v \\ rE \end{pmatrix}, \qquad \mathbf{E} = \begin{pmatrix} r\rho u \\ r(\rho u^2 + p) \\ r\rho v u \\ r\rho u H \end{pmatrix}$$
$$\mathbf{F} = \begin{pmatrix} r\rho v \\ r\rho u v \\ r(\rho v^2 + p) \\ r\rho v H \end{pmatrix}, \qquad \mathbf{S} = \begin{pmatrix} 0 \\ 0 \\ p \\ 0 \end{pmatrix} \tag{17}$$

where (u, v) are the velocity components in the (x, r) directions, and the total energy E is defined as

$$E = \frac{p}{\gamma - 1} + \frac{1}{2}\rho(u^2 + v^2) \tag{18}$$

In the axisymmetric description, the mass addition term does not appear in the source term, but it appears in the boundary conditions. The boundary conditions for the burning surface are given as

$$p(x, r_C(x), t) = p_w(x, t), \qquad T(x, r_C(x), t) = T_f(x, t)$$
$$\rho(x, r_C(x), t) = p_w(x, t)/(RT_f(x, t))$$
$$v(x, r_C(x), t) = -m_b(x, t)/\rho(x, r_C(x), t) \qquad \text{for } 0 \leq x \leq x_C \tag{19}$$

where the wall pressure p_w is the instantaneous local pressure on the burning surface and is approximated in the computation by the pressure of the finite volume cell adjacent to the burning surface. The flame temperature T_f and the mass generation rate m_b are given by solving the local thermal conduction problem inside the solid propellant with the present flame model.

For the inert wall, the boundary conditions are imposed as follows, assuming the specularly reflecting wall:

$$\frac{\partial \rho}{\partial n} = \frac{\partial p}{\partial n} = u_n = 0 \tag{20}$$

where n denotes the local normal direction of the wall.

3. Basic Equation for Thermal Conduction in the Solid Propellant

Let us assume, at each station of $x \leq x_C$, a semi-infinite, homogeneous solid propellant to burn in a one-dimensional manner to the negative direction of the y axis, that the local coordinate system is always fixed to the burning surface. The unsteady heat conduction in the solid propellant is described by the one-dimensional unsteady heat conduction equation:

$$\frac{\partial T}{\partial t} + \dot{r}_b \frac{\partial T}{\partial y} - \alpha_s \frac{\partial^2 T}{\partial y^2} = 0, \qquad t \geq 0, -\infty \leq y \leq 0 \tag{21}$$

where $T = T(y, t)$ is the temperature of the solid propellant, and α_s is the thermal diffusivity defined by

$$\alpha_s = \lambda_s/(\rho_s c_s) \tag{22}$$

where λ_s is the thermal conductivity and c_s is the specific heat.

The initial condition for the thermal equation is defined by the steady-state solution

$$T(y,0) = \bar{T}(y) = T_a + (T_{S0} - T_a)\exp\left(\frac{\dot{r}_{b0}}{\alpha_s} y\right) \tag{23}$$

for the boundary condition

$$\bar{T}(0) = T_{S0}, \qquad \bar{T}(-\infty) = T_a \tag{24}$$

where T_a is the initial temperature of the solid propellant.

The boundary conditions for the thermal conduction equation are defined as

$$T(-\infty, t) = T_a, \qquad T(0,t) = T_S(t) \tag{25}$$

$$\lambda_s \left.\frac{\partial T(y,t)}{\partial y}\right|_{y=-0} = \lambda_g \left.\frac{\partial T(y,t)}{\partial y}\right|_{y=+0} + \rho_s \dot{r}_b(t) Q_S \tag{26}$$

where the surface temperature $T_S(t)$ is an unknown value that must be determined at each moment through the simultaneous solution of the fluid dynamics and the thermal conduction. The thermal conduction coefficient of the gas is denoted by λ_g, and the heat release due to the surface reaction per unit mass of the generated gas is denoted by Q_S.

4. Quasi-Steady Flame Model

Let us consider the one-dimensional combustion region and assume it to be divided into a heating zone in a solid phase ($y < 0$), an exothermic reaction surface ($y = 0$), and a gaseous reaction zone ($0 < y \le \delta$), as shown in Fig. 2. There have been studies by many researchers on the flame models, and reviews on this topic are available [5,6]. The flame model employed here was first proposed in 1976 by Hanzawa [7,8] for the theoretical study on depressurization induced extinction of solid propellant. Within the flame layer of the thickness δ, which is considered to be very small, the nonconstant gaseous reaction is considered and the solution is integrated over the thickness to get the heat-feedback amount to the burning surface. It is also assumed that the reaction occurs through an irreversible pyrolysis process and the gas-phase reaction through a one-step-forward type of overall process between gaseous fuel and oxidizer, expressed as

$$\nu_F[F] + \nu_O[O] \rightarrow \nu_P[P] \tag{27}$$

where $[F]$, $[O]$, and $[P]$ denote fuel, oxidizer, and product, respectively. In this study, the stoichiometric mixture of the oxidizer and the fuel is considered. The Lewis number of the gas mixture is taken as unity. Furthermore, in the flame zone $0 \le y \le \delta$, the gas-phase processes are assumed to be quasi steady because the relaxation times of the processes are much smaller than those of the solid propellant thermal conduction and the gas dynamics in the chamber. The approximation is sometimes called t_C approximation [9], and the fundamental concept of it was put forward by Zel'dovich in 1942 [10]. The conservation equation in the flame zone for this case can be written neglecting the higher-order term of the injection velocity v as

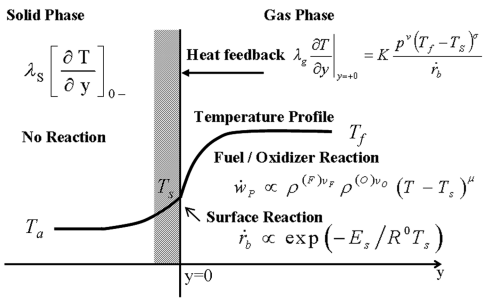

Fig. 2 Quasi-steady flame model.

$$\frac{\mathrm{d}\rho^{(P)}v}{\mathrm{d}y} - D\frac{\mathrm{d}^2\rho^{(P)}}{\mathrm{d}y^2} = \dot{w}^{(P)}, \qquad \frac{\mathrm{d}\rho v}{\mathrm{d}y} = 0, \qquad \frac{\mathrm{d}p}{\mathrm{d}y} = 0$$
$$c_p \frac{\mathrm{d}\rho v T}{\mathrm{d}y} - \lambda_g \frac{\mathrm{d}^2 T}{\mathrm{d}y^2} = \dot{w}^{(P)} Q \tag{28}$$

where $\rho = \rho^{(O)} + \rho^{(F)} + \rho^{(P)}$, D is the mass diffusion coefficient, $\dot{w}^{(P)}$ is the mass generation per unit time per unit volume, and Q is the heat generation due to the gas-phase reaction per unit mass of the product.

The boundary conditions for Eq. (28) are defined as

$$\left[(\rho^{(P)}v) - D\left(\frac{\mathrm{d}\rho^{(P)}}{\mathrm{d}y}\right)\right]_{y=+0} = 0$$
$$\left(\frac{\mathrm{d}\rho^{(P)}}{\mathrm{d}y}\right)_f = 0, \qquad \left(\frac{\mathrm{d}T}{\mathrm{d}y}\right)_f = 0 \tag{29}$$

$$-\lambda_g\left(\frac{\mathrm{d}T}{\mathrm{d}y}\right)_{y=+0} + \lambda_s\left(\frac{\mathrm{d}T}{\mathrm{d}y}\right)_{y=-0} = \rho_s \dot{r}_b Q_S \tag{30}$$

where the subscript f denotes where the gas-phase reaction completes (i.e., $y = \delta$). We obtain the following relation by integrating over Eq. (28) with the boundary conditions:

$$(\rho^{(P)}v)_f = \int_\delta \dot{w}^{(P)}\mathrm{d}y = (\rho v)_f = (\rho v)_S = \rho_s \dot{r}_b, \qquad p_f = p_S \tag{31}$$

$$c_p \rho_s \dot{r}_b (T_f - T_S) + \lambda_g\left(\frac{\mathrm{d}T}{\mathrm{d}y}\right)_{y=+0} = \rho_s \dot{r}_b Q \tag{32}$$

Eliminating the right-side (+) temperature gradient from Eqs. (30) and (32) and using the steady-state solution equation (23), we obtain

$$Q = -Q_s + c_p(T_{f0} - T_{S0}) + c_s(T_{S0} - T_a) \tag{33}$$

The linear burning rate is assumed to follow the Arrhenius-type function of the surface temperature and is defined as

$$\dot{r}_b(t) = \dot{r}_{b0}\exp\left[-\frac{E_s}{R^0}\left(\frac{1}{T_S(t)} - \frac{1}{T_{S0}}\right)\right] \tag{34}$$

where E_S is the activation energy and R^0 is the universal gas constant.

For the gas-phase reaction within the flame layer, we employ a polynomial form of the mass generation rate [7,8]:

$$w^{(P)} \propto (\rho^{(F)})^{\nu_F}(\rho^{(O)})^{\nu_O} T^{\mu'}(T - T_C)^{\mu} \tag{35}$$

The selection of this type is based on the fact that it can be made quite similar to the Arrhenius-type function with a proper choice of μ; furthermore, mathematical treatment becomes easier when the solution is integrated over the flame thickness δ. The parameter μ may be regarded as representing the activation energy of the reaction, and the T_C may be regarded as the ignition temperature of the gaseous reactants and set to the surface temperature T_S. Moreover, the amount of heat feedback [i.e., the right-side (+) temperature gradient at the burning surface] is expressed as follows:

$$\lambda_g \left.\frac{\partial T}{\partial y}\right|_{y=+0} = K\frac{p^{\nu}(T_f - T_S)^{\sigma}}{\dot{r}_b}$$
$$\sigma = \nu + \mu + 1, \nu = \nu^{(F)} + \nu^{(O)} \tag{36}$$

where K is a constant and is defined as

$$K = \frac{\rho_s r_{b0}^2}{p_0^{\nu}(T_{f0} - T_{S0})^{\sigma}}[c_s(T_{S0} - T_0) - Q_S] \tag{37}$$

This heat-feedback law was derived based on a distributed gas-phase reaction [7,8]. The case with a large value of σ represents a sharp flame or flame sheet, whereas the case in which $\sigma = 1$ corresponds to a uniform distribution of reaction rate. Although the latter heat-feedback law was first employed by Akiba and Tanno [11] to elucidate L^* combustion instability, it is often called the KTSS (Krier, T'ien, Sirignano, and Summerfield) model because Krier et al. [12] derived it theoretically for composite propellants. The preceding heat-feedback law accommodates both cases. This heat-feedback expression is useful for the fully coupled linear and nonlinear oscillatory combustion fluid dynamic computations. It has been used by the present authors for the nonlinear combustion instability problem [13]. In the present paper, we highlight the applicability of the scheme to the linear stability, which is the growth or the decay of an initially very small perturbation. It is one of the objectives of the study to show that we can conduct a simultaneous simulation of the unsteady fluid dynamics and the thermal conduction in an appropriate and less laborious fashion by making use of Eq. (36).

Eliminating the flame temperature T_f and the right-side (+) temperature gradient at the burning surface from Eqs. (30), (32), and (36), we obtain

$$\lambda_s \left(\frac{\mathrm{d}T}{\mathrm{d}y}\right)_{y=-0} = \frac{Kp^v}{\dot{r}_b c_p^\sigma}\left[Q + Q_S - \frac{\lambda_s}{\rho_s \dot{r}_b}\left(\frac{\mathrm{d}T}{\mathrm{d}y}\right)_{y=-0}\right]^\sigma + \rho_s \dot{r}_b Q_S \tag{38}$$

This equation implicitly defines the unique relationship between the left-side (−) temperature gradient and the surface temperature through the expression for $\dot{r}_b$ [Eq. (34)]. The quasi-steady surface temperature is determined in the simultaneous solution of the flowfield and the temperature distribution of the propellant using a one-sided finite difference approximation for the left-side (−) temperature gradient in Eq. (38), at each x station, and at each time stage.

B. Numerical Procedure

To visualize the effect of the precision of the numerical method on the present results, two kinds of methods are employed for computational fluid dynamics (CFD) computation. Moreover, the precision order was varied from first order to third order in both space and time. The RKDG method [14] is chosen for the platform for various precision calculations and the conventional FVM with second-order monotone upstream-centered scheme for conservation laws (MUSCL) approach is also tested. The local Lax–Friedrich scheme is used to evaluate the numerical convective flux at the cell interface. Recently, the application of the discontinuous Galerkin (DG) methods to the aeroacoustic problems have been studied eagerly by several researchers [15–17], but, as far as the authors know, the application of the DG method to the solid rocket motor internal unsteady flow is rare.

As for the thermal conduction in the solid propellant, the basic equation is nondimensionalized and converted through an exponential transformation and then discretized by the second-order finite difference method.

The temporal numerical integration is conducted by the total-variation-diminishing Runge–Kutta method.

1. *Discontinuous Galerkin Method*

The RKDG methods are stable, high-order accurate, and highly parallelizable schemes that can easily handle complicated geometries and boundary conditions. They are rather new, compared with the conventional FVM. Since the introduction of the method for the scalar problem in 1989 [18], they have been developed for various problems and used in a wide variety of applications. Today, they have made their way into the mainstream of computational fluid dynamics. The combination of a special class of Runge–Kutta time discretization and a finite element space discretization by discontinuous approximation with the ideas of numerical fluxes and slope limiters allows the method to be nonlinearly stable regardless of its accuracy. Please refer to an excellent review [14] written by the originators of the method for a detailed description.

In this study, the basic equations of fluid dynamics are discretized by the discontinuous Galerkin method for the ith space interval $[x_{i-1/2}, x_{i+1/2}]$ as

$$\int_{x_{i-1/2}}^{x_{i+1/2}} \frac{\partial \mathbf{q}_h(x,t)}{\partial t}\phi_i^\ell(x)\,\mathrm{d}x + \hat{\mathbf{f}}(\mathbf{q}_h(\bullet,t))\phi_i^\ell(x)\big|_{x_{i-1/2}}^{x_{i+1/2}} = \int_{x_{i-1/2}}^{x_{i+1/2}} (\mathbf{f}(\mathbf{q}_h(x,t))\frac{\mathrm{d}}{\mathrm{d}x}\phi_i^\ell(x) + \mathbf{S}(\mathbf{q}_h(x,t)))\,\mathrm{d}x \tag{39}$$

where $\mathbf{q}_h(x,t)$ is a discontinuous approximate solution in the ith space interval and is defined by the summation of the series of basic functions $\phi_i^\ell(x)$ $(\ell = 0, \ldots, k)$:

$$\mathbf{q}_h(x,t) = \sum_{\ell=0}^{k} \mathbf{q}_i^\ell(t)\phi_i^\ell(x) \tag{40}$$

where the Legendre polynomial functions P_ℓ are chosen for the basic functions;

$$\phi_i^\ell(x) \equiv P_\ell\left(\frac{2}{\Delta_i}(x - x_i)\right) \qquad x_{i-1/2} \le x \le x_{i+1/2},\ \Delta_i \equiv x_{i+1/2} - x_{i-1/2} \tag{41}$$

When we choose the Legendre polynomials as basis functions, the system of ordinary differential equations takes a particularly simple form, because we can use their L^2-orthogonality; that is,

$$\int_{-1}^{1} P_\ell(s)P_{\ell'}(s)\,\mathrm{d}s = \left(\frac{2}{2\ell+1}\right)\delta_{\ell\ell'} \tag{42}$$

A detailed description of the usefulness of the Legendre polynomials is available in [14] (pp. 187–188).

The numerical flux $\hat{\mathbf{f}}$ is calculated by the local Lax–Friedrich scheme:

$$\hat{\mathbf{f}}(\mathbf{q}_L, \mathbf{q}_R) = \tfrac{1}{2}[\mathbf{f}(\mathbf{q}_L) + \mathbf{f}(\mathbf{q}_R) - C(\mathbf{q}_R - \mathbf{q}_L)] \qquad C = \max[\Lambda_L, \Lambda_R] \tag{43}$$

where Λ is the spectral radius of the Jacobian matrix $\partial\mathbf{f}/\partial\mathbf{q}$. The values of $\mathbf{q}_L$ and $\mathbf{q}_R$ at a cell interface are determined from the local discontinuous solutions at the neighboring cells with the use of generalized slope limiters (see [14] for details).

The integral on the right-hand side of Eq. (39) is evaluated by the six-point Gauss–Legendre integration formula.

The value of k determines the order of accuracy of the method. The spatial accuracy is $k + 1$. The method includes conventional FVM in the case of $k = 0$. In the present study, the computational region in x direction is divided into 350 intervals with clustering grid points at the nozzle entrance region.

2. *Finite Volume Method with the Second-Order MUSCL Approach*

The basic equations of fluid dynamics are discretized for the ith space interval as

$$\Delta_i \frac{\mathrm{d}\mathbf{q}_i(t)}{\mathrm{d}t} + \hat{\mathbf{f}}(\mathbf{q}(\bullet,t))\big|_{x_{i-1/2}}^{x_{i+1/2}} = \mathbf{S}(\mathbf{q}_i(t))\Delta_i \qquad \mathbf{q}_i(x) \equiv \frac{1}{\Delta_i}\int_{x_{i-1/2}}^{x_{i+1/2}} \mathbf{q}(x,t)\,\mathrm{d}x \tag{44}$$

The physical values at cell interfaces are evaluated by the MUSCL approach with a slope limiter as

$$\mathbf{q}_L|_{i+1/2} = \mathbf{q}_i + m(\mathbf{q}_{i+1/2}^- - \mathbf{q}_i, \mathbf{q}_i - \mathbf{q}_{i-1}, \mathbf{q}_{i+1} - \mathbf{q}_i) \qquad \mathbf{q}_R|_{i-1/2} = \mathbf{q}_i - m(\mathbf{q}_i - \mathbf{q}_{i-1/2}^+, \mathbf{q}_i - \mathbf{q}_{i-1}, \mathbf{q}_{i+1} - \mathbf{q}_i) \tag{45}$$

where

$$m(a_1,a_2,a_3) = \begin{cases} s & \min_{1\le n\le 3}|a_n| \quad \text{if } s=\text{sign}(a_1)=\text{sign}(a_2)=\text{sign}(a_3) \\ 0 & \text{otherwise} \end{cases} \tag{46}$$

$$\mathbf{q}^{-}_{i+1/2} = \tfrac{1}{2}(3\mathbf{q}_i - \mathbf{q}_{i-1}), \qquad \mathbf{q}^{+}_{i-1/2} = \tfrac{1}{2}(3\mathbf{q}_i - \mathbf{q}_{i+1}) \tag{47}$$

3. Finite Difference Method for Thermal Conduction in the Solid Phase

The basic Eq. (21) is nondimensionalized as

$$\frac{\partial\theta}{\partial\hat{t}} + \hat{r}\frac{\partial\theta}{\partial\hat{y}} - \frac{\partial^2\theta}{\partial\hat{y}^2} = 0, \qquad \hat{t}\ge 0, \qquad -\infty \le \hat{y} \le 0 \tag{48}$$

through the following definitions:

$$\hat{y} = \frac{\dot{r}_{b0}}{\alpha_s}y, \qquad \hat{t} = \frac{t}{\alpha_s/\dot{r}_{b0}^2}, \qquad \hat{r} = \frac{\dot{r}_b}{\dot{r}_{b0}}, \qquad \theta = \frac{T-T_a}{T_{S0}-T_a} \tag{49}$$

The nondimensional boundary conditions are

$$\theta(-\infty,\hat{t}) = 0, \qquad \theta(0,\hat{t}) = \theta_S \equiv \frac{T_S - T_a}{T_{S0}-T_a} \tag{50}$$

$$\hat{K}\frac{\hat{p}^{\nu}}{\hat{r}}\left(\frac{c_s}{c_p}\right)^{\sigma}\left(\hat{Q}_S + \hat{Q} - \frac{\hat{b}}{\hat{r}}\right)^{\sigma} + \hat{r}\hat{Q}_S - \hat{b} = 0 \tag{51}$$

where

$$\hat{K} = \frac{1-\hat{Q}_S}{(\theta_{f0}-1)^{\sigma}}, \qquad \hat{Q} = \frac{c_p}{c_s}(\theta_{f0}-1) - \hat{Q}_S + 1$$
$$\hat{r} = \exp\left[-\hat{E}_s\frac{1-\theta_S}{\theta_S+\mu_a}\right] \tag{52}$$

$$\hat{b} \equiv \left.\frac{\partial\theta}{\partial\hat{y}}\right|_{\hat{y}=-0}, \qquad \hat{p} \equiv \frac{p}{p_0}, \qquad \mu_a \equiv \frac{T_a}{T_{S0}-T_a}$$
$$\hat{E}_s \equiv \frac{E_s}{R^0 T_{S0}} \tag{53}$$

$$\hat{Q}_S \equiv \frac{Q_S}{c_s(T_{S0}-T_a)}, \qquad \hat{Q} \equiv \frac{Q}{c_s(T_{S0}-T_a)}$$
$$\theta_{f0} \equiv \frac{T_{f0}-T_a}{T_{S0}-T_a} \tag{54}$$

The semi-infinite space $-\infty \le \hat{y} \le 1$ is transformed into a finite space $-1 \le \xi \le 0$ through the exponential coordinate transformation:

$$\xi = \exp(\beta\hat{y}) - 1 \tag{55}$$

where β is set to $\frac{1}{2}$ in this study. Then the basic equation is written in the transformed space as

$$\frac{\partial\theta}{\partial\hat{t}} + (\hat{r}-\beta)\beta(1+\xi)\frac{\partial\theta}{\partial\xi} - \beta^2(1+\xi)^2\frac{\partial^2\theta}{\partial\xi^2} = 0 \tag{56}$$

The steady-state solution is $\theta_0(\xi) = (1+\xi)^{1/\beta}$. In the boundary condition at $\xi = 0$,

$$\hat{b} \equiv \left.\frac{\partial\theta}{\partial\hat{y}}\right|_{\hat{y}=-0} = \beta\left.\frac{\partial\theta}{\partial\xi}\right|_{\xi=-0} \tag{57}$$

Discretization of the diffusion terms are approximated by the second-order central difference and the inertia term is approximated by the upwind difference. Then the final form of the discretization can be written as

$$\frac{\mathrm{d}\theta_j}{\mathrm{d}t} = \beta(1+\xi_j)\left[-(\hat{r}-\beta)\frac{\theta^n_{j+1}-\theta^n_{j-1}}{2\Delta} + \left\{\beta(1+\xi_j) + \frac{\Delta}{2}|\hat{r}-\beta|\right\}\frac{\theta^n_{j-1}-2\theta^n_j+\theta^n_{j+1}}{\Delta^2}\right] \tag{58}$$

where $\Delta \equiv 1/N_\xi$ is the equally divided interval of the computational space and is set to $1/50$ in this study.

4. Determination of the Surface Temperature and the Flame Temperature

The left-side (−) gradient of the nondimensional temperature at the burning surface is approximated by the one-sided finite difference scheme as

$$\hat{b} = \beta\frac{3\theta_S - 4\theta^n_{N_\xi} + \theta^n_{N_\xi-1}}{2\Delta} \tag{59}$$

This equation is combined with the boundary condition equation (51), and θ_S and $\hat{b}$ are solved by the Newton method. Then the flame temperature is calculated from

$$\theta_f = \frac{c_s}{c_p}\left(\hat{Q} + \hat{Q}_s - \frac{\hat{b}}{\hat{r}}\right) + \theta_S \tag{60}$$

The burning rate is calculated from Eq. (52). The burning rate and the flame temperature are dimensionalized and put into the source term of the basic equations of the Q1D fluid dynamics equation (9).

5. Total-Variation-Diminishing Runge–Kutta Time Discretization

In the preceding section, we derived the system of ordinary differential equations, then they were discretized in time by using the explicit high-order-accurate Runge–Kutta methods. They can be written for the first, second, and third orders as follows:

First order:

$$\mathbf{q}_h^{n+1} = \mathbf{q}_h^n + \Delta t^n L_h\left(\mathbf{q}_h^{(n)}\right) \tag{61}$$

Second order:

$$\mathbf{q}_h^{(1)} = \mathbf{q}_h^n + \Delta t^n L_h(\mathbf{q}_h^n), \qquad \mathbf{q}_h^{n+1} = \tfrac{1}{2}[\mathbf{q}_h^n + \mathbf{q}_h^{(1)} + \Delta t^n L_h(\mathbf{q}_h^{(1)})] \tag{62}$$

Third order:

$$\mathbf{q}_h^{(1)} = \mathbf{q}_h^n + \Delta t^n L_h\left(\mathbf{q}_h^n\right)$$
$$\mathbf{q}_h^{(2)} = \tfrac{1}{4}\left[3\mathbf{q}_h^n + \mathbf{q}_h^{(1)} + \Delta t^n L_h\left(\mathbf{q}_h^{(1)}\right)\right]$$
$$\mathbf{q}_h^{n+1} = \tfrac{1}{3}\left[\mathbf{q}_h^n + 2\left\{\mathbf{q}_h^{(2)} + \Delta t^n L_h\left(\mathbf{q}_h^{(2)}\right)\right\}\right] \tag{63}$$

C. Theoretical Evaluation

1. Burning-Rate Response Function

It is well known that the pressure-coupled burning-rate response function can be written as [9,19]

$$R_p \equiv \frac{\dot{r}'_b/\dot{r}_{b0}}{p'/p_0} = \frac{nAB}{\lambda + (A/\lambda) - (1+A) + AB} \tag{64}$$

Table 1 Values of combustion parameters

Properties	Value
ν	1.0
σ	4.0
T_a	300 K
T_{S0}	900 K
$\dot{r}_{b0}$	5×10^{-3} m/s
T_{f0}	2800 K
c_s, c_p	1381 J · K/kg
α_s	1.5×10^{-7} m^2/s
Q_S	248–610 kJ/kg
E_S/R^0	7500–12,000 K

$$\lambda = (1 + \sqrt{1 + 4\mathbf{i}\omega})/2, \qquad \omega = 2\pi f\left(\alpha_s/\dot{r}_{b0}^2\right) \tag{65}$$

where n is the pressure exponent of the steady-state burning-rate law, and f is the frequency. The parameters to determine the response functions can be calculated by the following expressions [20]:

$$A = \frac{E_S}{R^0 T_{S0}} \frac{T_{S0} - T_a}{T_{S0}}, \qquad B = \frac{2}{H} + \frac{1}{A}, \qquad n = \frac{\nu}{2 + (H/A)} \tag{66}$$

$$H = c_p(T_{S0} - T_a)\left[\frac{\sigma}{c_p(T_{f0} - T_{S0})} + \frac{1}{c_p(T_{S0} - T_0) - Q_S}\right] \tag{67}$$

For the present study, we employ the values shown in Table 1. In Fig. 3, the real part of the pressure-coupled response function is plotted for various values of Q_S, with E_S/R^0 fixed to 9000 K. It is clearly seen that the resonance frequency f_r is around 130 Hz for various values of Q_S. We chose the value of x_C as 4.15 m to satisfy Eq. (1).

2. Linear Growth Rate of the First Acoustic Mode

As the results of the linear theory [21], the linear growth rate of the first acoustic mode for the present situation can be written as

$$\begin{aligned}\alpha &= \alpha_C + \alpha_N + \alpha_{FT} \\ &= \frac{a_0\gamma}{R_C}\left[R_p^{(r)} - \frac{\gamma+2}{\gamma} + \left(\frac{T_f'/T_{f0}}{p'/p_0} - \frac{\gamma-1}{\gamma}\right)\right]M_{b0} \\ &\quad - \frac{a_0}{x_C}\frac{\gamma+1}{2}M_{N0} - \frac{a_0}{R_C}M_{b0} \\ &= \frac{a_0\gamma}{2x_C}\left[R_p^{(r)} - \frac{\gamma+2}{\gamma} + \left(\frac{T_f'/T_{f0}}{p'/p_0} - \frac{\gamma-1}{\gamma}\right)\right]M_{N0}\end{aligned} \tag{68}$$

where $R_p^{(r)}$ is the real part of the response function. The third relation is derived from the relationship between the burning surface Mach number M_{b0} and the nozzle entrance Mach number M_{N0}:

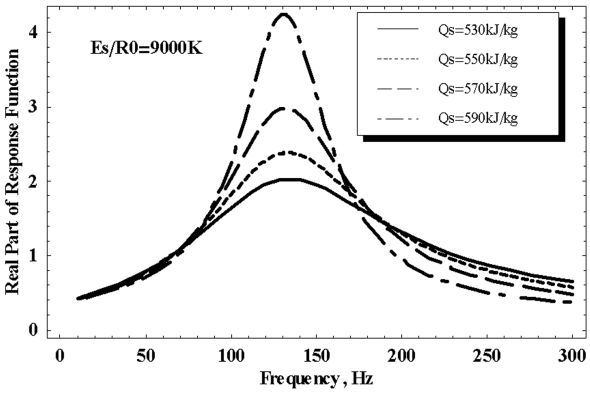

Fig. 3 Real part of the pressure-coupled response function.

$$M_{b0} = \frac{R_C}{2x_C}M_{N0} \tag{69}$$

The ratio of the flame temperature fluctuation intensity to that of the pressure, $(T_f'/T_{f0})/(p'/p_0)$ in Eq. (68), can be estimated by assuming the thermodynamic process in the flame. If the isentropic process is assumed, then one obtains

$$\frac{T_f'/T_{f0}}{p'/p_0} = \frac{\gamma - 1}{\gamma} \tag{70}$$

if the isothermal process is assumed, then

$$\frac{T_f'/T_{f0}}{p'/p_0} = 0 \tag{71}$$

and for the present flame model, we get

$$\frac{T_f'/T_{f0}}{p'/p_0} = \left(\frac{T_{S0} - T_a}{T_{f0}}\right)B\left(R_p^{(r)} - n\right) \tag{72}$$

The stability boundary can be obtained by applying the definition $\alpha = 0$ to Eq. (68).

III. Results and Discussion

A. Growth-Rate Evaluation

To evaluate the growth rate, the initial boundary problem described earlier was solved by the present numerical method. The initial perturbation is a cosine wave of the first acoustic mode and its initial amplitude is 0.1% of the chamber pressure p_c. The perturbation is superimposed on the steady-state solution, also obtained by the present numerical method. The history of the pressure at the head end of the chamber p_{HE} is used to evaluate the growth rate. The growth rate α (1/s) is evaluated by fitting the result with the function

$$\eta(\hat{t}) = Ce^{\hat{\alpha}\hat{t}} \tag{73}$$

where

$$\eta(\hat{t}) \equiv \frac{p_{\mathrm{HE}}(\hat{t})}{p_{0\mathrm{HE}}} - 1 \tag{74}$$

is the nondimensional acoustic pressure. The dimensional growth rate is evaluated as

$$\alpha = \hat{\alpha}\frac{\dot{r}_{b0}^2}{\alpha_s} \tag{75}$$

In Figs. 4 and 5, typical results are shown for the growing case and the decaying case. Two growth rates, α_1 and α_2, are estimated from the upper peak and the lower peak, respectively.

Several simulations were conducted by four kinds of discretization methods for the sets of combination of Q_S and M_{N0} with the activation energy set to 9000 K. Simulated cases and results of the growth rate are summarized in Table 2. These results of the growth rate are plotted against the nozzle entrance Mach number and compared with the linear theory in Fig. 6 for decaying cases and in Fig. 7 for growing cases, respectively. The values of the surface heat release Q_S for the decaying cases and the growing cases are chosen as 548,400 and 579, 800 kJ/kg, respectively. They are chosen from the vicinity of the stability boundary, as will be described in the next section.

The intensity of the growth rate becomes large as the nozzle entrance Mach number increases. From the results, it is clear that only the first-order scheme shows significant deviation from the others. There seems to be no possibility of the use of the first-order scheme. Though the third-order scheme shows the most reasonable results, its effect is not so significant. It is verified that the second-order FVM can be applied within a reasonable accuracy for the

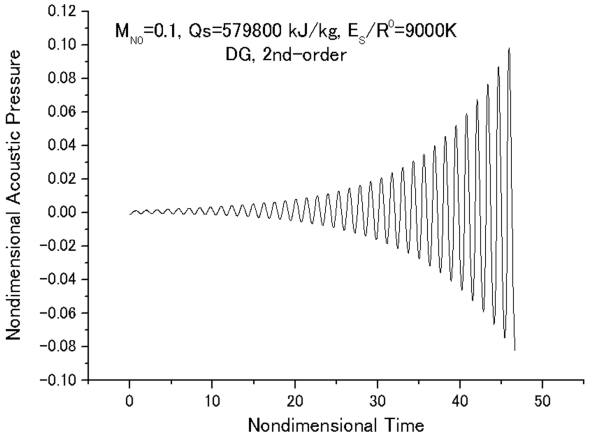

Fig. 4 Nondimensional acoustic pressure at the head end of the chamber: growing case.

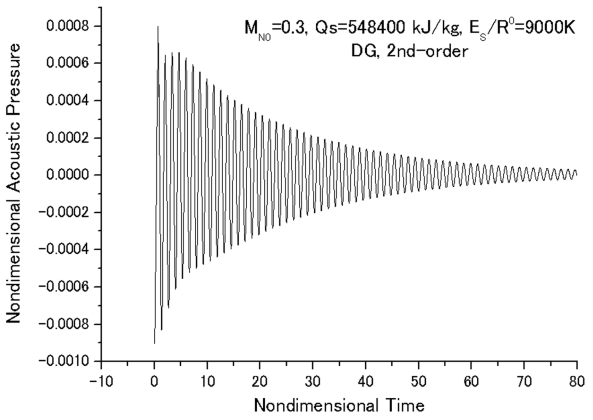

Fig. 5 Nondimensional acoustic pressure at the head end of the chamber: decaying case.

present problem. Currently, the accuracy control is made only for the fluid dynamic part of the simulation. It is natural to think that it is necessary to extend the control over the thermal conduction part before the final conclusion.

There is a common tendency that the present prediction gives moderate intensity of the growth rate compared with the linear theory for both growing and decaying cases. For the decaying case, the deviation between the theory and the simulation is small, such that a 2% decrease of the theoretical nozzle admittance can fill the difference. On the other hand, for the growing case, the difference from the linear theory becomes larger as the nozzle entrance Mach number increases. The reason for this can be attributed to the growth of the nonlinear effect for the higher Mach number in growing cases.

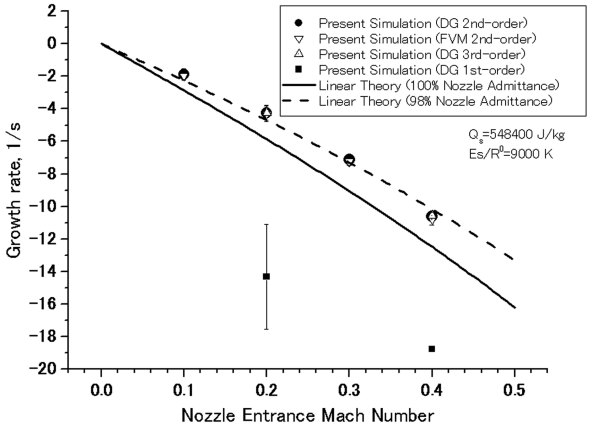

Fig. 6 Results of growth rate vs nozzle entrance Mach number: decaying cases.

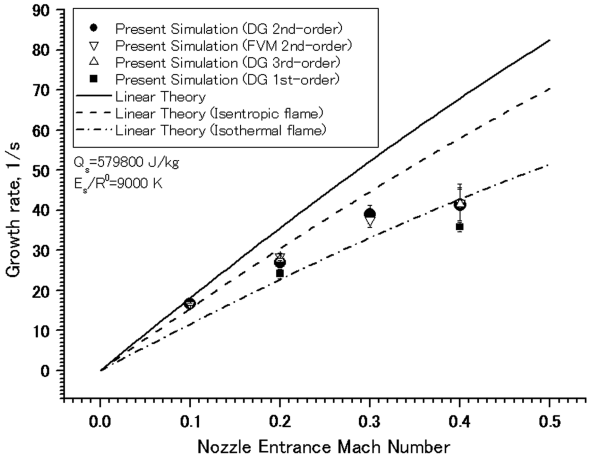

Fig. 7 Results of growth rate vs nozzle entrance Mach number: growing cases.

B. Stability Boundary

Because the nonlinear equations are solved directly in CFD, the influence from the terms of all the orders of the nozzle entrance Mach number is contained in the growth rate. On the other hand, in the linear analysis, only the first-order term of M_{N0} is considered. From the theoretical expression of the growth rate [Eq. (68)], we can evaluate the linear stability boundary. For example, for isentropic flame,

$$R_P^{(r)}|_{\text{stability boundary}} = \frac{\gamma + 2}{\gamma} \tag{76}$$

Table 2 Summary of growth-rate results for all simulation cases[a]

			Growth rate, 1/s							
			First-order DG		Second-order DG		Third-order DG		Second-order FVM	
E_S/R^0, K	Q_S, kJ/kg	M_{N0}	min	max	min	max	min	max	min	max
9000	548,400	0.1			−2.22	−1.54			−2.19	−1.95
9000		0.2	−17.5	−11.1	−4.75	−3.76	−4.67	−3.83	−4.79	−4.31
9000		0.3			−7.29	−6.97			−7.47	−7.23
9000		0.4	−18.8	−18.8	−10.7	−10.6	−10.7	−10.4	−11.1	−10.8
9000	579,800	0.1			16.5	16.8			16.2	16.8
9000		0.2	22.9	25.4	26.3	27.6	27.5	28.1	27.6	29.3
9000		0.3			36.6	41.3			35.8	39.2
9000		0.4	34.6	37.1	37.4	45.4	41.5	45.6	37.4	46.5

[a]DG is the discontinuous Galerkin method and FVM is the finite volume method.

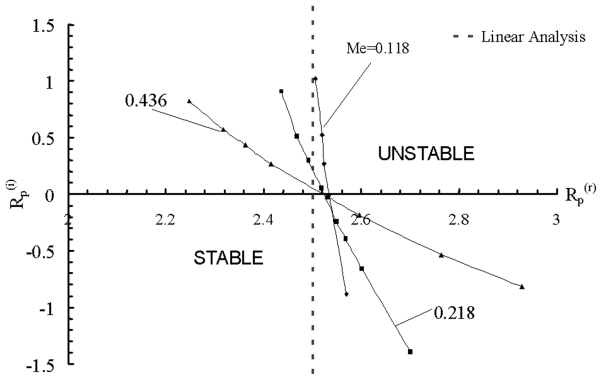

Fig. 8 Stability boundary by the linear analysis and the quasi-one-dimensional computation.

In Fig. 8, the stability limit obtained by the linear theory and that obtained by the present nonlinear computation are drawn as contour curves in the complex-response-function field for several values of the Mach number at the nozzle entrance. The simulation results for the cases were obtained [22–24] by the third-order FVM with the fourth-order Runge–Kutta explicit time discretization. The Roe scheme is used for the numerical flux. The region in x is divided into 1080 intervals nonuniformly, and 800 cells are used in the nozzle.

The stability limit of the linear analysis is shown by the dotted line, which is parallel to the imaginary-part axis. The numerical analysis result for a low Mach number ($M_{N0} = 0.118$) is close to the line. On the other hand, for the Mach number to become high, the stability-limit curve declines counterclockwise. This shows that the nonlinear stability limit depends on the imaginary part of the response function, too.

It is known from the linear analysis that the growth rate of the second order depends only on the imaginary part of the response function. Therefore, when the imaginary part of the response function vanishes, the growth rate depends only on the first-order, third-order, and higher-order terms. For the level of Mach number at the nozzle entrance, the third-order terms are one order smaller than the first-order term. Therefore, the growth rate substantially depends only on the first-order term; for that reason, it is thought that the curves of the stability boundary cross the real axis at a similar point.

C. Preliminary Results of Axisymmetric Simulations

It has been pointed out in the literature that there are physical limitations of the quasi-one-dimensional model. One of the most important mechanisms of multidimensional acoustic energy generation is the vortex-shedding phenomenon. Flandro and Jacobs [25], Flandro [26], Majdalani and Van Moorhem [27,28], and Kirkkopru et al. [29] resolved these more realistic transient-flow processes, addressing vorticity generation at injection surfaces due to an inviscid interaction between the acoustic pressure gradient imposed on the surface and the injected fluid. The basic point here is that a significant amount of energy is present in the vorticity disturbance relative to that in the acoustic disturbance. It follows that the classical irrotational linear stability theory cannot provide an accurate description of flow transients, because the rotational component of the flow disturbance is absent. Experiments [30,31] show that the vortex-shedding account is indispensable to explain the acoustic energy enhancement in segmented solid rocket motors.

The present preliminary axisymmetric calculations may include these effects, because the full Euler equations are used in the simulation. It should also be pointed out that in a model fully incorporating transverse (radial) effects, mass addition fluctuations are the source of axial acoustic disturbances in long, narrow chambers. This effect is seen indirectly in the quasi-one-dimensional model in Eq. (9), through the time dependence of the m_b term. Hence, in the present coupled model, one would find an acoustic disturbance field considerably more complex than that used in the quasi-one-dimensional model.

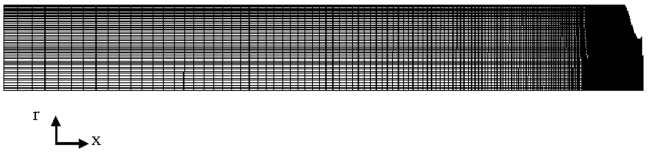

Fig. 9 Grid system for the axisymmetric case.

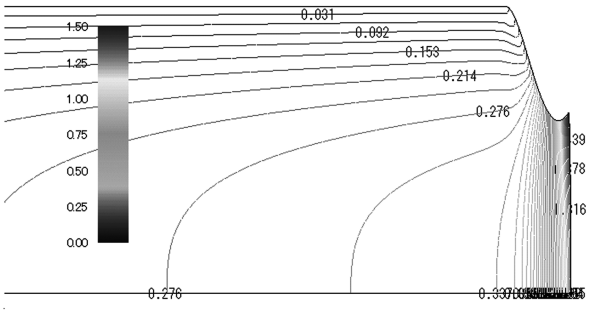

Fig. 10 Mach number contours near the aft end of the chamber.

The grid system used for the simulation consists of 340 points in the axial direction and 50 points in the radial direction for the fluid dynamic computation and is shown in Fig. 9. It should be noted that the axial scale and the radial scale are not the same, but the former is eight times more compressed than the latter.

Naturally, the axisymmetric flowfield differs substantially from that of the Q1D case as the Mach number contours, as shown in Fig. 10. Therefore, the comparison is made using the Mach number defined by the Q1D simulation for the common motor geometry.

The stability boundary for the case of axisymmetric flow is investigated under the conditions of the Q1D simulation and preliminary results are obtained [32]. Also, the growth rate as a function of the nozzle entrance Mach number is evaluated, and the results are compared with the linear analysis and the Q1D computation.

The results of the growth rate obtained by the axisymmetric simulation are shown in Figs. 11 and 12 for the decaying cases and the growing cases, respectively. Currently, axisymmetric results show stronger attenuation in both cases, especially at the higher Mach numbers. So far, detailed precision study has not been done on the axisymmetric simulations. Therefore, the reason for the discrepancy with Q1D cases may be attributed to the numerical dissipation that exists in the current FVM methods or in the grid system. It is worth trying to extend the higher-order RKDG scheme to the axisymmetric problems in the future.

For the Mach number beyond 0.3, the growth rate of the axisymmetric case notably decreases; although that symptom is also seen in the Q1D case, the degree of decaying is very significant. This may be attributed to the energy transfer to the radial mode excitation

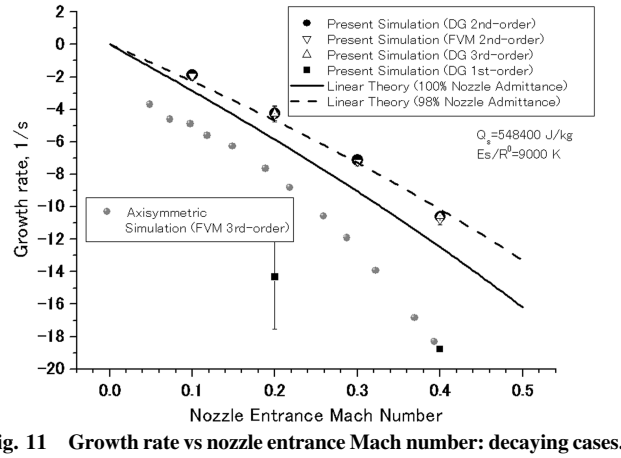

Fig. 11 Growth rate vs nozzle entrance Mach number: decaying cases.

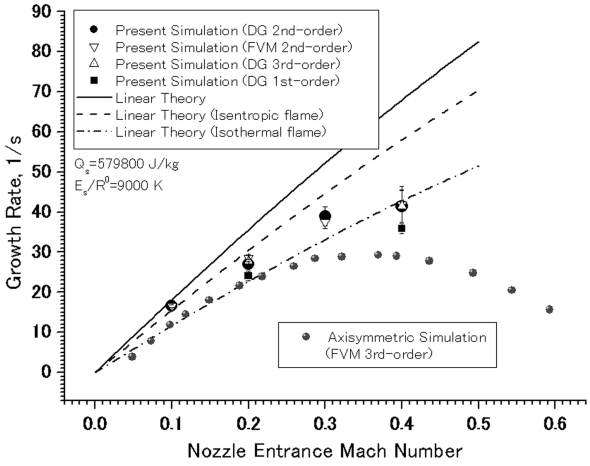

Fig. 12 Growth rate vs nozzle entrance Mach number: growing cases.

in the axisymmetric case, but, again, that is not easy to conclude, because the resonance frequency of the radial mode is higher than the axial frequency by the ratio of $x_C/(2R_C) \approx 30$ and cannot be activated easily.

IV. Conclusions

We developed a mathematical model and numerical schemes for the prediction of the linear stability of solid rocket motor combustion. The method is robust and accurate for the quasi-one-dimensional problems by the use of the quasi-steady flame model. Extension to the higher dimensions is straightforward, but current preliminary results show that careful examination of the numerical precision is necessary. In addition to this precision study, the inclusion of the particulates and efficient computational technique development are future challenges.

Acknowledgments

The authors would like to express sincere gratitude to the anonymous referees, without whose understanding and suggestions this paper could not have been completed. This research is partially supported by Japan Aerospace Exploration Agency (JAXA) grant U4-4K2- USRPJ-1002.

References

[1] Tseng, I. S., and Yang, V., "Interactions of Homogeneous Propellant Combustion and Acoustic Waves in a Solid Rocket Motor," AIAA Paper 92-0101, 1992.

[2] Chibli, H. A., Majdalani, J., and Flandro, G. A., "Fundamental Growth Rate Corrections in Rocket Motor Stability Calculations," AIAA Paper 2002-3610, 2002.

[3] Zinn, B. T., "Longitudinal Mode Acoustic Losses in Short Nozzles," *Journal of Sound and Vibration*, Vol. 22, No. 1, 1972, pp. 93–105. doi:10.1016/0022-460X(72)90847-4

[4] Kooker, D. E., and Zinn, B. T., "Triggering Axial Instabilities in Solid Rockets: Numerical Predictions," 9th AIAA/SAE Propulsion Conference, Las Vegas, NV, AIAA Paper 73-1298, Nov. 1973.

[5] De Luca, L., "Theory of Nonsteady Burning and Combustion Stability of Solid Propellants by Flame Models," *Nonsteady Burning and Combustion Stability of Solid Propellants*, edited by De Luca, L., Price, E. W., and Summerfield, M., Progress in Astronautics and Aeronautics, Vol. 143, AIAA, Reston, VA, 1992, pp. 519–600.

[6] Jackson, T. L., Massa, L., and Brewster, M. Q., "Unsteady Combustion Modelling of Energetic Solids, Revisited," *Combustion Theory and Modeling*, Vol. 8, No. 3, 2004, pp. 513–532. doi:10.1088/1364-7830/8/3/005

[7] Hanzawa, M., "A Theoretical Study on the Extinction of Solid Propellants by a Rapid Pressure Decay," Ph.D. Dissertation, Univ. of Tokyo, Tokyo, Japan, 1976.

[8] Hanzawa, M., "A Theoretical Study on Depressurization Induced Extinction of Solid Propellant," AIAA/SAE 12th Propulsion Conference, AIAA Paper 76-635, 1976.

[9] Novozhilov, B. V., "Theory of Nonsteady Burning and Combustion Stability of Solid Propellant by the Zeldovich–Novozhilov Method," *Nonsteady Burning and Combustion Stability of Solid Propellant*, Progress in Astronautical and Aeronautics, Vol 143, AIAA, Reston, VA, 1992, pp. 601–641.

[10] Zel'dovich, Ya. B., "On the Theory of Propellant Combustion," *Zhurnal Eksperimental'noi i Teoreticheskoi Fiziki*, Vol. 12, Nos. 11–12, 1942, p. 498.

[11] Akiba, R., and Tanno, M., "Low Frequency Instability in Solid Propellant Rocket Motors," *Proceedings of the First International Symposium on Rockets and Astronautics*, Japanese Rocket Society, Tokyo, 1959, pp. 74–82.

[12] Krier, H., T'ien, J. S., Sirignano, W. A., and Summerfield, M., "Non-Steady Burning Phenomena of Solid Propellants: Theory and Experiments," *AIAA Journal*, Vol. 6, No. 2, 1968, pp. 278–285.

[13] Morita, T., Hanzawa, M., and Shimada, T., "CFD Analyses of Low Frequency Combustion Instability in Solid Propellant Rocket Motors," *Advancements in Energetic Materials and Chemical Propulsion*, edited by K. K. Kuo and J. de Dios Rivera, Begell House, New York, 2007, pp. 457–475.

[14] Cockburn, B., and Shu, C.-W., "Runge–Kutta Discontinuous Galerkin Methods for Convection-Dominated Problems," *Journal of Scientific Computing*, Vol. 16, No. 3, 2001, pp. 173–261. doi:10.1023/A:1012873910884

[15] Peyret, C., and Delorme, Ph., "HP Discontinuous Galerkin Method for Computational Aeroacoustics," 13th AIAA/CEAS Aeroacoustics Conference, Rome, AIAA Paper 2007-3475, May 2007.

[16] Loercher, F., Gassner, G., and Munz, C.-D., "The Space-Time Discontinuous Galerkin Method for the Solution of Unsteady Compressible Navier–Stokes Equations," 13th AIAA/CEAS Aeroacoustics Conference, Rome, AIAA Paper 2007-3477, May 2007.

[17] Gabard, G., "Wave-Based Discontinuous Galerkin Methods for the Linearized Euler Equations in the Frequency Domain," 13th AIAA/CEAS Aeroacoustics Conference, Rome, AIAA Paper 2007-3476, May 2007.

[18] Cockburn, B., and Shu, C.-W., "TVB Runge–Kutta Local Projection Discontinuous Galerkin Finite Element Method for Conservation Laws 2: General Framework," *Mathematics of Computation*, Vol. 52, No. 186, 1989, pp. 411–435. doi:10.2307/2008474

[19] Culick, F. E. C., "A Review of Calculations for Unsteady Burning of a Solid Propellant," *AIAA Journal*, Vol. 6, No. 12, 1968, pp. 2241–2255.

[20] King, M. K., "Composite Propellant Combustion Modeling," AIAA/SAE/ASME 16th Joint Propulsion Conference, Hartford, CT, AIAA Paper 80-1124, June 1980.

[21] Culick, F. E. C., and Yang, V., "Prediction of Stability of Unsteady Motions in Solid Propellant Rocket Motors," *Nonsteady Burning and Combustion Stability of Solid Propellant*, Progress in Astronautics and Aeronautics, Vol. 143, AIAA, Reston, VA, 1992, pp. 719–804.

[22] Kato, T., Hanzawa, M., Morita, T., and Shimada, T., "Stability Evaluation of One-Dimensional Flow in Solid Rocket Motors Based on Computational Fluid Dynamics," *Proceedings of Asian Joint Conference on Propulsion and Power*, Seoul National Univ., Seoul, Korea, 2004, pp. 84–91.

[23] Kato, T., Hanzawa, M., Yoshikawa, T., and Shimada, T., "CFD Analysis of One-Dimensional Combustion Instability in Solid Rocket Motors," *Asian Joint Conference on Propulsion and Power* [CD-ROM], Japan Society for Aeronautical and Space Sciences, Tokyo, 2005.

[24] Yoshikawa, T., Shimada, T., Wada, Y., and Hanzawa, M., "Stability Analysis of Solid Rocket Motor Internal Flow by Computational Fluid Dynamics," *Symposium on Space Transportation*, Inst. of Space and Astronautical Science, JAXA, Kanagawa, Japan, Jan. 2006, pp. 21–24 (in Japanese).

[25] Flandro, G. A., and Jacobs, H. R., "Vortex Generated Sound in Cavities," AIAA Aeroacoustics Conference, Seattle, WA, AIAA Paper 73-1014, Oct. 1973.

[26] Flandro, G. A., "Vortex Driving Mechanism in Oscillatory Rocket Flows," *Journal of Propulsion and Power*, Vol. 2, No. 3, 1986, pp. 206–214.

[27] Majdalani, J., and Van Moorhem, W. K., "A Multiple-Scales Solution to the Acoustic Boundary Layer in Solid Rocket Motors," *Journal of Propulsion and Power*, Vol. 13, No. 2, March 1997, pp. 186–193.

[28] Majdalani, J., and Van Moorhem, W. K., "An Improved Time-Dependent Flowfield Solution for Solid Rocket Motors," 33rd AIAA/ASME/SAE/ASEE Joint Propulsion Conference and Exhibit, Seattle, WA, AIAA 97-2717, July 1997.

[29] Kirkkopru, K., Kassoy, D. R., and Zhao, Q., "Unsteady Vorticity Generation and Evolution in a Model of a Solid Rocket Motor: Sidewall

Mass Addition Transients," AIAA 33rd Aerospace Sciences Meeting and Exhibit, Reno, NV, AIAA Paper 95-0603, Jan. 1995.

[30] Brown, R. S., Dunlap, R., Young, S. W., and Waugh, R. C., "Vortex Shedding as a Source of Acoustic Energy in Segmented Solid Rockets," *Journal of Spacecraft and Rockets*, Vol. 18, No. 4, 1981, pp. 312–319.

[31] Vetel, J., Plourde, F., Doan-Kim, S., and Guery, J-F., "Experimental and Numerical Characterizations of Unstable Sources in a Solid Rocket Motor," 37th AIAA/ASME/SAE/ASEE Joint Propulsion Conference and Exhibit, Salt Lake City, UT, AIAA Paper 2001-3866, July 2001.

[32] Yoshikawa, T., "Stability Analysis of Solid Rocket Motor Internal Flow by Computational Fluid Dynamics," M.S. Thesis, Tokai Univ., Kanagawa, Japan, 2005 (in Japanese).

T. Jackson
Associate Editor